

CONRAD-2: the new neutron imaging instrument at the Helmholtz-Zentrum Berlin

Nikolay Kardjilov,^{a*} André Hilger,^a Ingo Manke,^a Robin Woracek^{a,b,c} and John Banhart^a

^aInstitute of Applied Materials (EM-IAM), Helmholtz-Zentrum Berlin für Materialien und Energie, Hahn-Meitner Platz 1, Berlin, 14109, Germany, ^bEngineering Science, University of Tennessee, 325 John D Tickle Building, Knoxville, Tennessee 37996, USA, and ^cInstrument Department, European Spallation Source (ESS), Lund, Sweden. *Correspondence e-mail: kardjilov@helmholtz-berlin.de

Received 23 July 2015

Accepted 5 December 2015

Edited by A. J. Allen, National Institute of Standards and Technology, Gaithersburg, USA

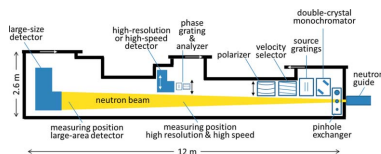
Keywords: neutron imaging; neutron tomography; Bragg-edge imaging; instrumentation.

The construction of the new neutron imaging instrument at the BER-2 research reactor of the Helmholtz-Zentrum Berlin has greatly increased the potential of the facility. The redesign of the facility included improvements of the neutron extraction and transportation systems, more effective shielding, and innovative instrumentation. The cold neutron flux at the neutron guide exit was increased by more than one order of magnitude, which allowed for an implementation of methods that require monochromatic or polarized beams, thus enabling the exploitation of nonconventional contrast mechanisms such as phase, diffraction and magnetic contrasts. The improved instrument design also facilitates the development of high-resolution neutron tomography by providing an increased beam intensity at the sample position.

1. Introduction

Neutron imaging is an experimental method for the nondestructive investigation of the internal structure of materials or engineering components and can be applied to a broad range of problems in materials research and fundamental science (Strobl, Manke *et al.*, 2009; Kardjilov, Manke *et al.*, 2011; Lehmann, 2008). The method has been implemented at various large-scale neutron sources where dedicated imaging facilities have been installed (Hussey *et al.*, 2005; Kaestner *et al.*, 2011). Such installations are being used for the research of the beamline owners ('in-house research') as well as for projects of researchers from other institutions including commercial organizations. The design and the performance of such an instrument has to meet all the requirements related to the fields of application envisaged and should also provide opportunities for innovative instrument development.

Besides conventional imaging based on absorption contrast, new experimental methods have been implemented within the past few years at neutron imaging facilities, which exploit other interaction mechanisms of neutrons with matter. Those contrast mechanisms and methods include phase contrast (Allman *et al.*, 2000), differential phase contrast (Pfeiffer *et al.*, 2006), (ultra)-small-angle scattering by dark-field imaging (Strobl *et al.*, 2008) and (in the future) by spin-echo modulations (Strobl *et al.*, 2012), magnetic contrast by polarized neutron imaging (Kardjilov *et al.*, 2008), and diffraction contrast by Bragg-edge imaging (Kockelmann *et al.*, 2007; Woracek *et al.*, 2011, 2014; Lehmann *et al.*, 2009). Neutron resonance absorption imaging can be utilized at upcoming imaging instruments at spallation sources (Tremisn *et al.*, 2012). In order to accommodate all these methods at a single



© 2016 International Union of Crystallography

instrument, a large degree of flexibility and modularity is necessary. The presence of a broad spectrum of cold neutrons is an essential condition for exploiting the wave nature of the neutron and thus enabling interaction mechanisms such as coherent neutron scattering, wave propagation with phase shifts and magnetic moment precession in external magnetic fields.

CONRAD-2 is well suited for absorption contrast radiography and tomography and is frequently used for basic science and industrial applications, while allowing energy-selective measurements with no additional effort. Furthermore, solid-state polarizers can be installed and used for imaging with polarized neutrons (Wood & Anderson, 2001). Phase grating setups are available and can be used for grating interferometry experiments, where phase contrast and dark-field imaging are used to obtain spatially resolved information about the microstructure or magnetic properties of materials (Pfeiffer *et al.*, 2006; Kardjilov *et al.*, 2008).

2. Instrument parameters

The imaging facility at the BER II research reactor was designed in 2004 and constructed in 2005 as an instrument supporting the materials research activities at the former Hahn-Meitner-Institute (Kardjilov, Hilger *et al.*, 2011). At that time, V7 (CONRAD-1) was situated at the neutron guide NL-1B (^{58}Ni coated) with a characteristic wavelength of 2.2 Å. The space behind the neutron guide did not allow for a long collimation path, since only 5 m of unoccupied space was available. Therefore, the beam size at the sample position was limited to 10 × 10 cm (Kardjilov, Hilger *et al.*, 2011). This size was too small for many conventional imaging purposes and was a competitive disadvantage compared to other existing facilities worldwide.

The upgrade program of CONRAD-1 (V7) between October 2010 and October 2012 included (i) an exchange of the ^{58}Ni -coated neutron guides ($m = 1.2$, which allows for reflection of neutrons with 1.2 times the divergence compared to using a mirror based on a single Ni layer) with new supermirror guides ($m = 2.5$ or 3 in the curved section and $m =$

2 in the following straight section; see Fig. 1), (ii) an increase of the collimation path from 5 m to 10 m, and (iii) the provision of a more spacious experimental environment and user work space. These upgrades improved the efficiency of neutron transport and led to an increased beam size owing to the larger beam divergence and longer collimation path. Additionally, the curvature of the guide was increased by changing the curvature radius from $R = 3000$ m to $R = 750$ m in order to enlarge the distance from the shielding of the neighboring instrument to the beam axis.

The new neutron guide design is presented in Fig. 1.

Monte Carlo simulations showed that using a curved guide section with a length of 15 m and a radius of $R = 750$ m is sufficient to avoid a direct line of sight to the cold source of the reactor. The optimization study of the curved guide section indicated that different wall coatings ($m = 2.5$ for the inner wall and $m = 3.0$ for the outer, top and bottom walls) provide the best result in terms of transported beam intensity and homogeneity. In front of and behind the curved guide are straight guide sections, as shown in Fig. 1. The role of the final straight section is to homogenize the beam intensity over the guide cross section. All guide sections have a constant cross section of height × width = 12 × 3 cm.

A flight path of $L = 12$ m is available downstream of the final straight guide section. This distance is necessary in order to make full use of the pinhole configuration, where a certain L/D ratio can be realized by using apertures with different diameter D at the beginning of the flight path. For apertures with typical diameters of 1–3 cm, the calculated L/D ratios are between 1200 and 400, respectively.

The complete layout of the CONRAD-2 instrument is shown in Fig. 2. The shielding of the instrument hutch is based on a sandwich design where the inner side is covered by 5 mm of B_4C plastic and the outer side is shielded by 5–10 cm-thick lead plates.

In the presented instrument's layout three sections which are accessible through slide doors (shown as arrows) can be defined. In the first section the beam modulation is performed by using a pinhole exchanger for setting different L/D ratios, a double-crystal monochromator and a velocity selector for

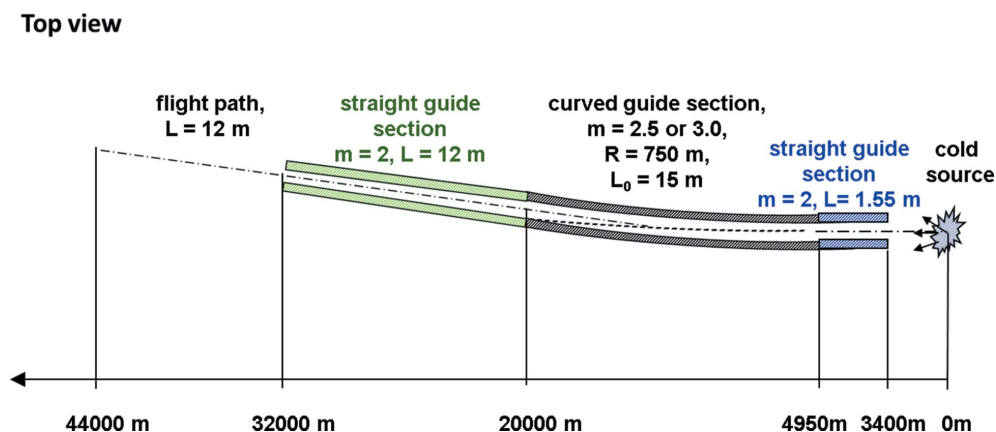


Figure 1 Neutron guide design of the CONRAD-2 neutron imaging instrument. View from the top.

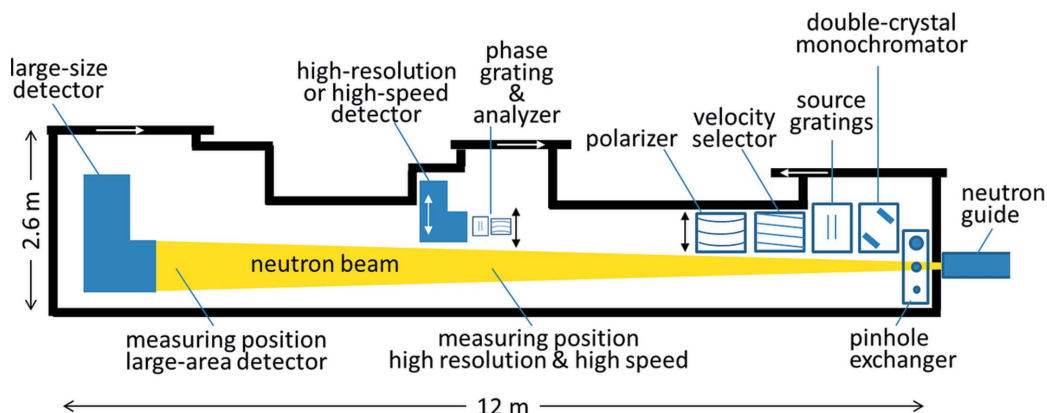


Figure 2
Layout of the neutron imaging instrument CONRAD-2.

extraction of monochromatic beams, a source grating setup for grating interferometry, and a polarizer for imaging with polarized neutrons. These devices can be placed in the beam by translation stages, and the combination of a few devices is possible (e.g. grating interferometry with a monochromatic beam). In the second section a measuring position for high-resolution and high-speed imaging is installed, because of the narrow and intense beam which is available there. Depending on the used option a small pinhole can be set by the pinhole exchanger in order to provide a well collimated beam in the case of high-resolution measurements or a larger aperture can be used in the case of dynamic imaging. In addition, the analyzer for polarized neutrons or the phase grating for the grating interferometry technique can be used in front of the detector. The sample environment and the detector can be translated out of the beam if measurements at the end position are performed. At a distance of 12 m from the pinhole the beam expands to 30×30 cm owing to the divergence provided by the neutron guide. This position is used for investigation of large samples. The paths between the three positions are covered by aluminium containers (length of 1 m each) filled with He gas in order to prevent intensity losses by scattering of neutrons in air. Nevertheless the containers can be removed separately and the free space can be used as a temporary measuring position. This opportunity is used when dynamic studies with short exposure times are performed. In this case the measuring position is placed as close as possible to the neutron guide.

After completion of the upgrade, the intensity at the end of the guide (at the pinhole position) was 13.5 times the previously measured intensity, with a flux of 2.7×10^9 n cm⁻² s⁻¹. The intensity measured at the end position 10 m from the pinhole was 2.4×10^7 n cm⁻² s⁻¹ at an L/D set to 330 (pinhole $D = 3$ cm). The illuminated area was markedly increased, now allowing us to investigate samples up to 30×30 cm in size. Additional scanning of the sample with image stitching even permits imaging of samples up to 50×50 cm large.

To characterize the intensity distribution of the beam, images of the empty beam were acquired at the sample position (10 m distance from the pinhole position) by a position-

sensitive (two-dimensional) detector (Williams *et al.*, 2012; Kardjilov, Dawson *et al.*, 2011; Tötzke *et al.*, 2011) (see Fig. 3). The instrument is equipped with different detector systems optimized for large size samples (large area detector: sCMOS Andor ‘Neo’ 2560×2160 pixel; 50, 100 or 200 μm ⁶LiZnS:Ag scintillators), for visualization of dynamic processes (high speed detector: sCMOS Andor ‘Neo’ 2560×2160 pixel; 200 or 400 μm ⁶LiZnS:Ag scintillators) and for high-resolution imaging, where a prototype of a high-resolution detector (CCD Andor ‘DW436N-BC’ 2048×2048 pixel; 10 μm Gd₂O₂S scintillator) provides images of samples with a pixel size as low as 6.4 μm at reasonable exposure times (Williams *et al.*, 2012). The different detector systems available at the beamline are summarized in Table 1.

Imaging facilities located at neutron guides in general suffer from a non-uniform intensity distribution and a pronounced dispersion of neutron divergences introduced by reflections in

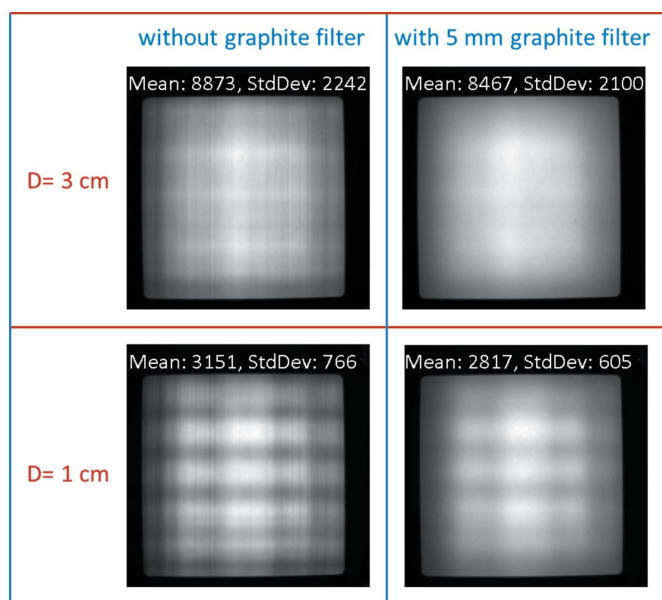


Figure 3
Images of the primary beam applying different pinhole diameters D and an optional graphite filter. The size of the illuminated area is 20×20 cm.

Table 1
Parameters of the detector systems available at the imaging instrument CONRAD-2.

Detector	Field of view (cm)	Pixel size (μm)	Exposure time (s)
High resolution	1.3 (diameter)	6.4	5–60
High speed	Up to 10×10	15–40	0.005–1
Large area	Up to 30×30	40–117	1–60

the guide, especially at guide intersections. Therefore the resulting images contain corresponding line patterns which become more pronounced when the L/D ratio is increased, e.g. by decreasing the pinhole size. This effect is illustrated in Fig. 3, where images of the primary beam were taken with pinhole sizes D of either 1 or 3 cm and optionally using a 5 mm-thick graphite filter (a polydisperse powder) acting as a diffuser as a possible remedy. The graphite powder was compacted into an Al box of 5×5 cm cross section and placed between the guide end and the pinhole.

The measured mean values over the various images in Fig. 3 show that the 5 mm-thick graphite filter reduces the neutron flux by 5–10% but significantly improves the beam homogeneity, which can be seen by the decrease of the standard deviation of the pixel values in the illuminated area.

The neutron beam wavelength spectrum at the instrument was measured by using a time-of-flight technique, utilizing a double-slit chopper disc rotating at 25 Hz and a time resolving ^3He counter detector placed at 5 m distance from the chopper.

The spectral distribution presented in Fig. 4 shows that the cold neutron beam contains contributions in a wavelength interval from 1 to 11 Å with a maximum at 2.5 Å. Thermal and epithermal neutrons below 1 Å are completely absent owing to the curved neutron guide section used, which filters out not only the high-energy neutrons but also the direct γ radiation from the reactor core. The dip observed at 4.5 Å is due to the presence of the monochromator of the diffraction instrument placed upstream of CONRAD-2, which removes some of the neutrons. Unlike at CONRAD-1 this contribution is constant and can be easily accounted for.

Besides conventional imaging applications using a polychromatic neutron beam, the instrument is designed for experiments requiring monochromatic beams. For this purpose, a double-crystal monochromator was installed at the end of the neutron guide system in combination with a

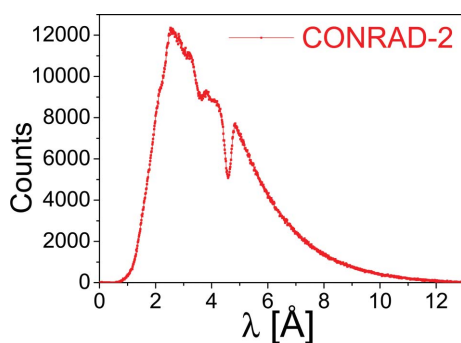


Figure 4
Wavelength spectrum of the neutron beam used by the CONRAD-2 imaging instrument as measured at the end of the neutron guide.

Table 2
Parameters of the two available monochromatic devices available at the imaging instrument CONRAD-2.

Device	Selectable wavelength interval (Å)	Energy resolution, $\Delta\lambda/\lambda$ (%)
Velocity selector	3.5–6	15
Double-crystal monochromator with pyrolytic graphite crystals (0.8° mosaicity)	1–6	3

pinhole, as shown in Fig. 5. This configuration allows for remotely switching between monochromatic and polychromatic neutron beams and also for defining a certain L/D ratio.

Fig. 5 shows the two configurations of the beam extraction module. The first configuration allows for the extraction of a monochromatic beam by the double-crystal monochromator arrangement. The second configuration provides a polychromatic beam at the same beam position by opening a pinhole and moving the upper monochromator out of the beam. Hence, the switch from a monochromatic to a polychromatic beam can be done without having to move the sample. The wavelength can be adjusted continuously between 1 and 6 Å, while the beam path remains unchanged. To achieve this, the same rotation angle is chosen for the upper and lower crystals, while positioning the lower crystal on a linear stage.

Another option for beam monochromatization is the utilization of a velocity selector. The velocity selector can be placed in the polychromatic beam 1.5 m from the pinhole (see Fig. 2). The parameters of the two available setups are given in Table 2.

V7 (CONRAD-1) has been widely recognized as a versatile and flexible instrument for innovative neutron imaging and has helped to make decisive contributions to the development of new methods by exploiting different contrast mechanisms. One reason for the success in method development was the

Side view

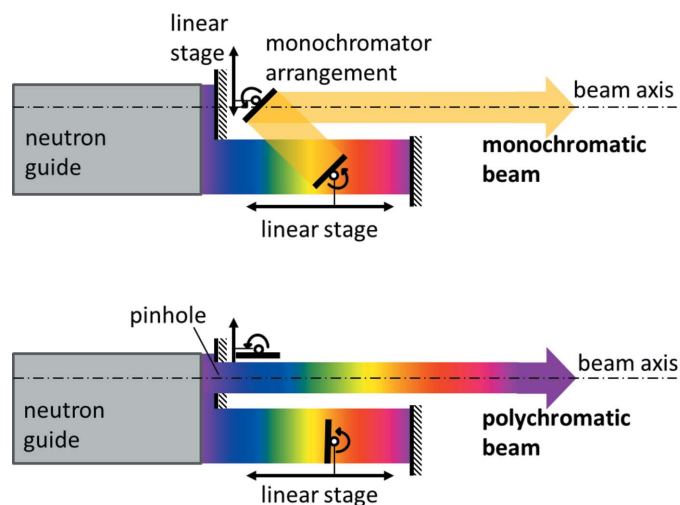


Figure 5
Sketch of the monochromator installed at the imaging instrument CONRAD-2. Two modes of operation are shown: (top) monochromatic beam is produced, (bottom) polychromatic beam passes the device.

flexibility of the facility, permitting users to quickly change the instrument's configuration and allowing for the performance of nonstandard experiments.

3. Selection of applications

The range of applications of CONRAD-2 will be demonstrated by showing examples ranging from ordinary absorption contrast tomography to various scientifically promising fields that exploit contrast mechanisms based on diffraction, neutron phase shift or magnetic interactions of polarized neutrons with matter.

3.1. Absorption contrast imaging

Typical absorption contrast applications are related to cases where X-ray imaging methods fail to provide the required contrast, either because of the sample thickness or because individual chemical elements in the sample have too similar attenuation coefficients. The high sensitivity of neutrons to hydrogen and lithium favors the investigation of devices and components related to the fuel cell and lithium ion battery industries (Hickner *et al.*, 2006; Boillat *et al.*, 2010; Markötter *et al.*, 2012; Owejan *et al.*, 2012). Neutron imaging is well suited for the investigation of dynamic processes in hydrogen storage materials as well (Gondek *et al.*, 2011; Pohlmann *et al.*, 2015; Herbrig *et al.*, 2015). The high penetration depth of a neutron beam into metals combined with high-resolution imaging enables researchers to trace crack initiation in welded materials or during fatigue testing. An example of hydrogen embrittlement and blistering in an electrochemically charged iron sample is shown in Fig. 6 (Griesche, Dabah, Kardjilov *et al.*, 2014; Griesche, Dabah, Kannengiesser *et al.*, 2014).

The high-resolution detector system at the CONRAD-2 instrument made it possible to observe cracks filled with molecular hydrogen as shown in Fig. 6. After the sample had been annealed at 353 K, neutron tomography showed the release of the hydrogen. Digital alignment of the three-

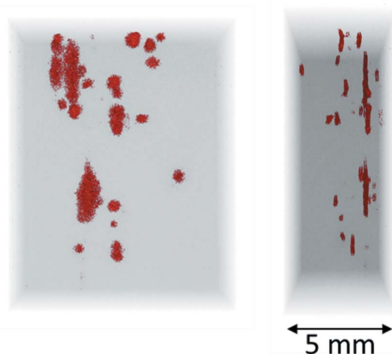


Figure 6

Example of high-resolution neutron tomography of hydrogen embrittlement and blistering in an electrochemically charged iron sample. The three-dimensional volume rendering of the tomographic data allows for the introduction of color coding, where the highly attenuating hydrogen gas in the cracks is marked in red and the iron matrix is set as semitransparent.

dimensional sample volumes before and after the annealing process allows for a quantification of the amount of hydrogen in the cracks.

3.2. Diffraction contrast imaging at the Bragg edges

In (poly)crystalline materials, the neutron beam attenuation coefficient owes some of its wavelength dependence to the fact that some neutrons are scattered out of the incident beam by Bragg diffraction (Fermi *et al.*, 1947; Winsberg *et al.*, 1949). At certain wavelengths, in analogy to Bragg peaks in a diffractometer (occurring for different wavelengths when the scattering angle is constant), Bragg edges are observed in the transmission spectrum. Analysis of Bragg edges has been notably exploited in time-of-flight mode at neutron spallation sources (Vogel, 2000; Santisteban *et al.*, 2001; Steuwer, 2002). The associated imaging method is hence often termed 'Bragg-edge imaging' (Kockelmann *et al.*, 2007; Woracek *et al.*, 2014; Lehmann *et al.*, 2009; Kardjilov *et al.*, 2012) and can be carried out in a few different ways (Lehmann *et al.*, 2009) by using

(a) the time-of-flight method (using a pulsed neutron beam) and a suitable time-resolved imaging detector,

(b) a velocity (turbine blade) selector,

(c) the 'slit method', where several monochromator crystals reject the unwanted energies and the transmitted beam is used, and

(d) a tunable monochromator crystal (typically a double-crystal monochromator where the incident beam direction remains unchanged).

At CONRAD-2 a velocity selector and double-crystal monochromator are available (see Table 2). Since in imaging mode the detector is positioned behind the sample, the probed scattering angle is equivalent to $2\theta = 180^\circ$. For a given hkl family of lattice planes, the scattering angle increases as the wavelength is increased until the Bragg scattering condition can no longer be fulfilled by any orientation of a crystallite in the sample. This occurs for wavelengths larger than $\lambda = 2d_{hkl}\sin 90^\circ = 2d_{hkl}$. At this particular wavelength, the transmitted intensity increases markedly, forming the so-called Bragg edge. The corresponding absorbance decreases and is characteristic for different crystallographic structures [see Fig. 7(a) for an example of austenite and martensite]. Phase, texture and strain differences within a sample will lead to variations in the Bragg-edge spectrum and can be spatially resolved using an imaging detector (Woracek *et al.*, 2014, 2011; Santisteban *et al.*, 2011).

A recent study at CONRAD-2 showcased the use of this technique by separating and quantifying different crystallographic phases in metastable stainless steel (ASTM standard 304L) that exhibits the TRIP effect (Woracek *et al.*, 2014). Several samples were subjected to certain plastic tensile and torsional strains, inducing a martensitic phase transformation, where austenite (having a face-centered cubic structure, fcc) transforms to martensite (consisting of body-centered cubic, bcc, and hexagonal close packed, hcp, structures). Radiographs of samples with varying amounts of austenite and martensite were recorded at several wavelengths. Fig. 7(b) shows the transmission spectra obtained for three different

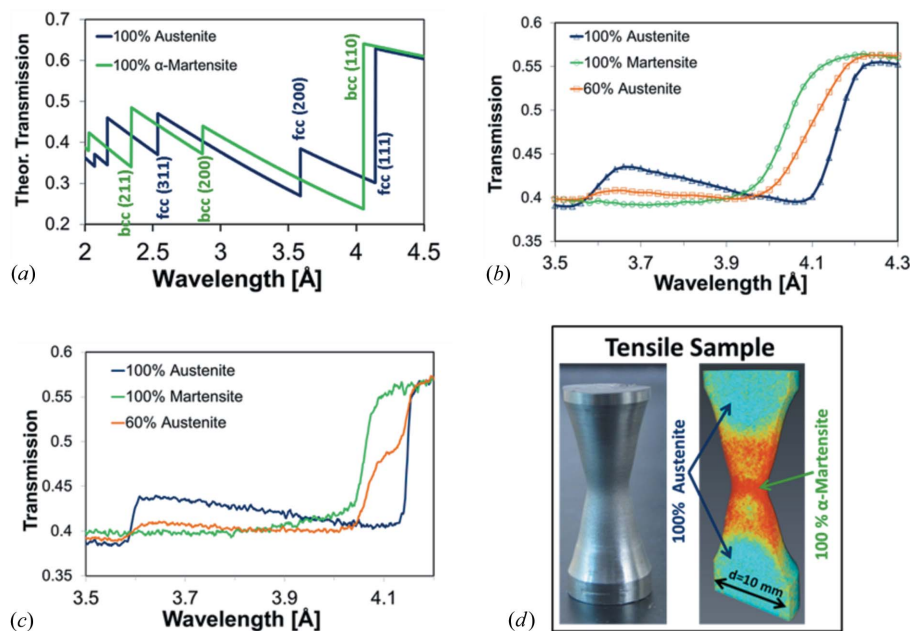


Figure 7
 Example of energy-selective imaging. (a) Theoretical transmission values for austenite and α -martensite. (b) Experimentally measured transmission spectra at CONRAD-2 for iron samples of varying phase compositions. (c) A comparison of the same samples measured in time-of-flight mode at a spallation source with better wavelength resolution. (d) Three-dimensional reconstructed phase fractions, obtained at CONRAD-2, inside a plastically deformed tensile sample, where large plastic deformation leads to the formation of martensite.

samples (regions) with a thickness of 8 mm, where the wavelength increment between each radiograph was 0.02 \AA and the integration time for each image was 2 min. As a reference, Fig. 7(c) shows an example of transmission spectra obtained for the same samples in time-of-flight mode at a spallation source with an energy resolution of 0.4%, where a shoulder-like double edge is visible for the sample with 60% austenite. However, phase discrimination is also possible with the reduced resolution of the monochromator, even though only one Bragg edge is visible around the ‘Bragg cut off’ for mixed phases. The position (and rise) of this observed edge is directly influenced by the phase fraction. At CONRAD-2, tomographic scans were performed by recording 180 projections over a 360° range below (4.1 \AA) and above (4.3 \AA) the Bragg edge corresponding to the fcc(111) lattice planes of the austenitic phase. The exposure times were 2 min per projection, resulting in a total measurement time of 12 h for both wavelengths. The filtered back-projection algorithm for parallel beam reconstruction was used to reconstruct the tomographic data sets.

At 4.1 \AA , the attenuation coefficient for regions with larger martensitic phase content is lower than for regions with more austenitic phase content, owing to the differing Bragg-edge positions. By normalizing the reconstructed data taken at 4.1 \AA by the data taken at 4.3 \AA , a ratio of the Bragg-edge height is obtained that can be used for quantification of the phase fractions. Neutron diffraction was used at selected locations inside the samples, while electron backscatter

diffraction was used on the surface of cut cross sections to verify the neutron-imaging-based results. All results show very good agreement (Woracek *et al.*, 2015).

Diffraction contrast imaging at the Bragg edges with monoenergetic neutrons can therefore be used as a complementary visualization and quantification tool to study phase transition effects in steels and other metals. It allows for nondestructive bulk investigations and can reveal inhomogeneities that may remain undetected if only diffraction is used, while other features visible in the tomography data (such as cracks, porosities *etc*) can be visualized simultaneously.

3.3. Grating interferometry and imaging with polarized neutrons

As discussed, neutron imaging can be combined with experimental techniques which allow for exploiting contrasts different from the classical attenuation contrast. Here we give a short description of two more methods without going into great detail but

providing some essential references.

Neutrons obey the particle–wave dualism and can be described as a propagating wave, which is an essential condition to perform phase-contrast-based techniques. An example of this is the grating interferometry technique which can be used to characterize heterogeneities on scales from 0.1 to $10 \text{ }\mu\text{m}$ (Hilger *et al.*, 2010; Strobl, Hilger *et al.*, 2009). Refraction at the magnetic domain walls can be used to visualize magnetic domains (Grunzweig *et al.*, 2008; Manke *et al.*, 2010; Lee *et al.*, 2010). Using tomographic reconstruction, the three-dimensional domain network can be analyzed and studied. The future improvement of the spatial resolution of detector systems will allow for accessing finer domain arrangements which will help in investigating the shape, size and distribution of individual domains in bulk materials.

The magnetic moment of the neutron makes it sensible to magnetic fields, allowing one to visualize the field inside and outside of bulky samples. Magnetic imaging has some tantalizing prospects for future studies of magnetic phenomena throughout science and technology: the establishment and trapping of magnetic flux in superconductors below the critical temperature (Dawson *et al.*, 2009), the skin effect in conductors (Manke *et al.*, 2008) and magnetic field distributions around conductors (Strobl, Kardjilov *et al.*, 2009). In some cases, the method can also be extended to three dimensions in analogy to standard tomography. To achieve this, the development of advanced algorithms for tomographic reconstruction of complex vector magnetic fields is underway.

4. Discussion and conclusions

A major upgrade of the neutron tomography instrument at the neutron source BER-2 has led to the versatile, flexible and modular facility CONRAD-2, with an associated improvement of most of the beamline parameters of the predecessor instrument CONRAD-1. The recent development of methods such as imaging with polarized neutrons, grating interferometry and Bragg-edge mapping has already shown the potential of the new imaging instrument CONRAD-2 and these techniques have already been implemented there. The next important step is to identify further scientific and industrial problems to which these methods can be applied in a sense that they provide unique results which are not obtainable by other experimental methods. The increase of spatial resolution is a major trend in imaging in general and also in neutron imaging. The beam characteristics of CONRAD-2 allow for achieving this goal. The ongoing detector development at the facility has already provided promising results and the continuation of this activity is important for the instrument as well as for the neutron imaging community. The trend towards time-of-flight imaging is important in relation to projects for constructing imaging beamlines at new neutron spallation sources (ESS, SNS, J-PARC and ISIS). In addition to this trend, the strength of energy-selective imaging at continuous sources can be emphasized (Hilger *et al.*, 2015). The stable beam, the excellent signal-to-noise ratio and the easier data treatment provide good arguments for further development of this method at continuous neutron sources.

References

- Allman, B. E., McMahon, P. J., Nugent, K. A., Paganin, D., Jacobson, D. L., Arif, M. & Werner, S. A. (2000). *Nature*, **408**, 158–159.
- Boillat, P., Frei, G., Lehmann, E. H., Scherer, G. G. & Wokaun, A. (2010). *Electrochem. Solid-State Lett.* **13**, B25–B27.
- Dawson, M., Manke, I., Kardjilov, N., Hilger, A., Strobl, M. & Banhart, J. (2009). *New J. Phys.* **11**, 043013.
- Fermi, E., Sturm, W. J. & Sachs, R. G. (1947). *Phys. Rev.* **71**, 589–594.
- Gondek, L., Selvaraj, N. B., Czub, J., Figiel, H., Chapelle, D., Kardjilov, N., Hilger, A. & Manke, I. (2011). *Int. J. Hydrogen Energy*, **36**, 9751–9757.
- Griesche, A., Dabah, E., Kannengiesser, T., Kardjilov, N., Hilger, A. & Manke, I. (2014). *Acta Mater.* **78**, 14–22.
- Griesche, A., Dabah, E., Kardjilov, N., Hilger, A., Manke, I. & Kannengiesser, T. (2014). *Int. J. Mater. Res.* **105**, 640–644.
- Grünzweig, C., David, C., Bunk, O., Dierolf, M., Frei, G., Kühne, G., Kohlbrecher, J., Schafer, R., Lejcek, P., Ronnow, H. M. R. & Pfeiffer, F. (2008). *Phys. Rev. Lett.* **101**, 025504.
- Herbrig, K., Pohlmann, C., Gondek, Ł., Figiel, H., Kardjilov, N., Hilger, A., Manke, I., Banhart, J., Kieback, B. & Röntzsch, L. (2015). *J. Power Sources*, **293**, 109–118.
- Hickner, M. A., Siegel, N. P., Chen, K. S., McBrayer, D. N., Hussey, D. S., Jacobson, D. L. & Arif, M. (2006). *J. Electrochem. Soc.* **153**, A902–A908.
- Hilger, A., Kardjilov, N., Kandemir, T., Manke, I., Banhart, J., Penumadu, D., Manescu, A. & Strobl, M. (2010). *J. Appl. Phys.* **107**, 036101.
- Hilger, A., Kardjilov, N., Manke, I., Zandler, C., Lieutenant, K., Habicht, K., Banhart, J. & Strobl, M. (2015). *Opt. Express*, **23**, 301–311.
- Hussey, D. S., Jacobson, D. L., Arif, M., Huffman, P. R., Williams, R. E. & Cook, J. C. (2005). *Nucl. Instrum. Methods Phys. Res. Sect. A*, **542**, 9–15.
- Kaestner, A. P., Hartmann, S., Kühne, G., Frei, G., Grünzweig, C., Josic, L., Schmid, F. & Lehmann, E. H. (2011). *Nucl. Instrum. Methods Phys. Res. Sect. A*, **659**, 387–393.
- Kardjilov, N., Dawson, M., Hilger, A., Manke, I., Strobl, M., Penumadu, D., Kim, K. H., Garcia-Moreno, F. & Banhart, J. (2011). *Nucl. Instrum. Methods Phys. Res. Sect. A*, **651**, 95–99.
- Kardjilov, N., Hilger, A., Manke, I., Strobl, M., Dawson, M., Williams, S. & Banhart, J. (2011). *Nucl. Instrum. Methods Phys. Res. Sect. A*, **651**, 47–52.
- Kardjilov, N., Manke, I., Hilger, A., Strobl, M. & Banhart, J. (2011). *Mater. Today*, **14**, 248–256.
- Kardjilov, N., Manke, I., Hilger, A., Williams, S., Strobl, M., Woracek, R., Boin, M., Lehmann, E., Penumadu, D. & Banhart, J. (2012). *Int. J. Mater. Res.* **103**, 151–154.
- Kardjilov, N., Manke, I., Strobl, M., Hilger, A., Treimer, W., Meissner, M., Krist, T. & Banhart, J. (2008). *Nat. Phys.* **4**, 399–403.
- Kockelmann, W., Frei, G., Lehmann, E. H., Vontobel, P. & Santisteban, J. R. (2007). *Nucl. Instrum. Methods Phys. Res. Sect. A*, **578**, 421–434.
- Lee, S. W., Kim, K. Y., Kwon, O. Y., Kardjilov, N., Dawson, M., Hilger, A. & Manke, I. (2010). *Appl. Phys. Expr.* **3**, 106602.
- Lehmann, E. (2008). *Pramana J. Phys.* **71**, 653–661.
- Lehmann, E. H., Frei, G., Vontobel, P., Josic, L., Kardjilov, N., Hilger, A., Kockelmann, W. & Steuwer, A. (2009). *Nucl. Instrum. Methods Phys. Res. Sect. A*, **603**, 429–438.
- Manke, I., Kardjilov, N., Schäfer, R., Hilger, A., Strobl, M., Dawson, M., Grünzweig, C., Behr, G., Hentschel, M., David, C., Kupsch, A., Lange, A. & Banhart, J. (2010). *Nat. Commun.* **1**, 125.
- Manke, I., Kardjilov, N., Strobl, M., Hilger, A. & Banhart, J. (2008). *J. Appl. Phys.* **104**, 076109.
- Markötter, H., Manke, I., Kuhn, R., Arlt, T., Kardjilov, N., Hentschel, M. P., Kupsch, A., Lange, A., Hartnig, C., Scholta, J. & Banhart, J. (2012). *J. Power Sources*, **219**, 120–125.
- Owejan, J. P., Gagliardo, J. J., Harris, S. J., Wang, H., Hussey, D. S. & Jacobson, D. L. (2012). *Electrochim. Acta*, **66**, 94–99.
- Pfeiffer, F., Grünzweig, C., Bunk, O., Frei, G., Lehmann, E. & David, C. (2006). *Phys. Rev. Lett.* **96**, 215505.
- Pohlmann, C., Herbrig, K., Gondek, Ł., Kardjilov, N., Hilger, A., Figiel, H., Banhart, J., Kieback, B., Manke, I. & Röntzsch, L. (2015). *J. Power Sources*, **277**, 360–369.
- Santisteban, J. R., Edwards, L., Steuwer, A. & Withers, P. J. (2001). *J. Appl. Cryst.* **34**, 289–297.
- Santisteban, J. R., Vicente-Alvarez, M. A., Vizcaino, P., Banchik, A. D., Vogel, S. C., Tremsin, A. S., Vallerga, J. V., McPhate, J. B., Lehmann, E. & Kockelmann, W. (2011). *J. Nucl. Mater.* **425**, 218.
- Steuwer, A. (2002). Thesis, University of Cambridge, UK.
- Strobl, M., Grünzweig, C., Hilger, A., Manke, I., Kardjilov, N., David, C. & Pfeiffer, F. (2008). *Phys. Rev. Lett.* **101**, 123902.
- Strobl, M., Hilger, A., Kardjilov, N., Ebrahimi, O., Keil, S. & Manke, I. (2009). *Nucl. Instrum. Methods Phys. Res. Sect. A*, **605**, 9–12.
- Strobl, M., Kardjilov, N., Hilger, A., Jericha, E., Badurek, G. & Manke, I. (2009). *Phys. B Condens. Matter*, **404**, 2611–2614.
- Strobl, M., Manke, I., Kardjilov, N., Hilger, A., Dawson, M. & Banhart, J. (2009). *J. Phys. D Appl. Phys.* **42**, 243001.
- Strobl, M., Wieder, F., Duif, C. P., Hilger, A., Kardjilov, N., Manke, I. & Bouwman, W. G. (2012). *Phys. B Condens. Matter*, **407**, 4132–4135.
- Tötzke, C., Manke, I., Hilger, A., Choinka, G., Kardjilov, N., Arlt, T., Markötter, H., Schröder, A., Wippermann, K., Stolten, D., Hartnig, C., Krüger, P., Kuhn, R. & Banhart, J. (2011). *J. Power Sources*, **196**, 4631–4637.
- Tremsin, A. S., McPhate, J. B., Vallerga, J. V., Siegmund, O. H. W., Kockelmann, W., Schooneveld, E. M., Rhodes, N. J. & Feller, W. B. (2012). *IEEE Trans. Nucl. Sci.* **59**, 3272–3277.
- Vogel, S. (2000). Dissertation thesis, University of Kiel, Germany.

- Williams, S. H., Hilger, A., Kardjilov, N., Manke, I., Strobl, M., Douissard, P. A., Martin, T., Riesemeier, H. & Banhart, J. (2012). *J. Instrum.* **7**, P02014.
- Winsberg, L., Meneghetti, D. & Sidhu, S. S. (1949). *Phys. Rev.* **75**, 975–979.
- Wood, J. L. & Anderson, I. S. (2001). Editors. *Neutron Optics*. Bellingham: SPIE.
- Woracek, R., Penumadu, D., Kardjilov, N., Hilger, A., Boin, M., Banhart, J. & Manke, I. (2014). *Adv. Mater.* **26**, 4069–4073.
- Woracek, R., Penumadu, D., Kardjilov, N., Hilger, A., Boin, M., Banhart, J. & Manke, I. (2015). *Phys. Procedia*, **69**, 227–236.
- Woracek, R., Penumadu, D., Kardjilov, N., Hilger, A., Strobl, M., Wimpory, R. C., Manke, I. & Banhart, J. (2011). *J. Appl. Phys.* **109**, 093506.